

# Simultaneous Incorporation of V and Mn Element into Polyanionic NASICON for High Energy-Density and Long-Lifespan Zn-Ion Storage

Zeyi Wu, Fei Ye, Qiang Liu, Ruilvjing Pang, Yang Liu, Le Jiang, Zilong Tang, and Linfeng Hu\*

Aqueous Zn-ion battery (AZIB) has attracted huge attention due to its distinct advantages such as abundant zinc sources, low development cost, high security, and environmental friendliness compared to traditional commercialized batteries. Developing novel cathode materials with high energy density and long lifespan is very important for the practical application of AZIB in the coming years. Herein, V and Mn elements are simultaneously incorporated into the NASICON host to make use of the electrochemical redox reaction in both V and Mn transition metal elements for aqueous Zn-ion storage. A significant increase in both capacity and working voltage has been observed after Mn doping into  $\text{Na}_3\text{V}_2(\text{PO}_4)_3$  to form  $\text{Na}_4\text{VMn}(\text{PO}_4)_3$ . Taking advantage of the merits of both high capacity and high voltage, the  $\text{Na}_4\text{VMn}(\text{PO}_4)_3$ @Graphene cathode delivers an optimal energy density of  $309.7 \text{ Wh kg}^{-1}$  with very stable cycle performance (89.1% capacity retention after 3000 cycles at  $5.0 \text{ A g}^{-1}$ ). A two-step electron transfer mechanism between  $\text{V}^{4+}/\text{V}^{3+}$  and  $\text{Mn}^{3+}/\text{Mn}^{2+}$  redox couple in  $\text{Na}_4\text{VMn}(\text{PO}_4)_3$  has been revealed during the electrochemical process for Zn-ion storage.

energy technology.<sup>[1]</sup> Recently, beyond LIBs ( $\text{Na}^+$ ,  $\text{K}^+$ ,  $\text{Mg}^{2+}$ ,  $\text{Ca}^{2+}$ ,  $\text{Zn}^{2+}$ ,  $\text{Al}^{3+}$ ) batteries have attracted great attention.<sup>[2,3]</sup> Among them, aqueous Zn-ion batteries (AZIBs) shows apparent merits of abundant zinc sources, low development cost, high security, and environmental friendliness. More importantly, the chemical stability of metal zinc in a water-oxygen environment is much superior than other alkali metals and polyvalent metals, thus in favor of the design of aqueous batteries.<sup>[4,5]</sup> However, the revolution of AZIBs is still at its early stage and far from the practical application because of the lack of suitable cathode materials. The relatively high redox potential of  $\approx -0.76 \text{ V}$  (vs NHE) of  $\text{Zn}^{2+}/\text{Zn}$  generally calls for high-voltage cathodes to construct an aqueous battery with satisfying energy density.<sup>[6]</sup>

Recently, polyanionic compounds consisting of alternately linked  $[\text{XO}_4]$  ( $\text{X} = \text{P}$ ,  $\text{S}$ ,  $\text{Si}$ , etc.) tetrahedron and  $[\text{MO}_6]$  ( $\text{M} = \text{V}$ ,  $\text{Mn}$ ,  $\text{Fe}$ ,  $\text{Co}$ ,  $\text{Cr}$ , etc.) octahedron have been developed as very promising candidates for AZIBs cathode. Profiting from the inductive effect on the M–O bond and the binding effect on oxygen atoms originating from the presence of  $[\text{XO}_4]$ , polyanionic compounds generally combine the disadvantages of a high discharged plateau and excellent thermal stability.<sup>[7–9]</sup> Typically, a series of V-based phosphate based polyanionic compounds have been reported for the construction of ZIBs cathode materials such as layered hydrated  $\text{VOPO}_4$  and NASICON-typed  $\text{Na}_3\text{V}_2\text{PO}_4$ .<sup>[10,11]</sup> For instance, Huang et al. revealed that NASICON-typed  $\text{Na}_3\text{V}_2(\text{PO}_4)_3$  displays a specific capacity of  $\approx 100 \text{ mAh g}^{-1}$  and a satisfying plateau of  $\approx 1.1 \text{ V}$  when served as a ZIBs cathode.<sup>[11]</sup> Our previous work also revealed layered hydrated  $\text{VOPO}_4 \cdot 2\text{H}_2\text{O}$  as high voltage cathode materials originated from the aforementioned inductive effect.<sup>[12–14]</sup> Nevertheless, in spite of the high voltage plateau and decent cyclability, relative low specific capacity (generally  $< 150 \text{ mAh g}^{-1}$ ) of V-based phosphate based polyanionic compounds is still a huge obstacle for the realization of high energy density cathode.<sup>[12,15,16]</sup>

It is known that V and Mn are two important active metal elements in most of AZIBs cathode materials. This inspired us to consider whether one can incorporate V and Mn elements simultaneously into polyanionic compounds hosts to

## 1. Introduction

Electrochemical energy storage plays an especially vital role due to its steady and convenient power supply for portable devices and smart electronics. Commercial lithium-ion batteries (LIBs) suffers from drawbacks including limited lithium resources and potential security are still a practical obstacle for new

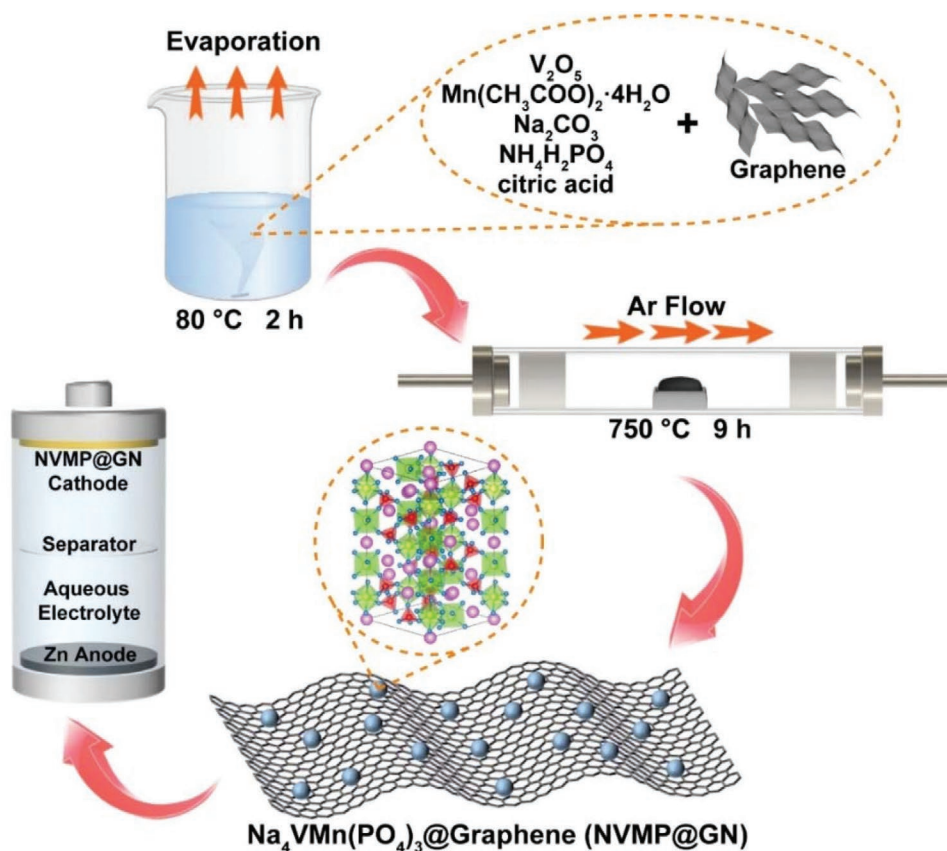
Z. Y. Wu, L. Jiang  
Department of Materials Science  
Fudan University  
Shanghai 200433, P. R. China

F. Ye, Q. Liu, R. L. J. Pang, Y. Liu, L. F. Hu  
School of Materials Science and Engineering  
Southeast University  
Nanjing 211189, P. R. China  
E-mail: linfenghu@seu.edu.cn

Z. L. Tang  
State Key Laboratory of New Ceramics and Fine Processing  
School of Materials Science and Engineering  
Tsinghua University  
Beijing 100084, China

 The ORCID identification number(s) for the author(s) of this article can be found under <https://doi.org/10.1002/aenm.202200654>.

DOI: 10.1002/aenm.202200654



**Scheme 1.** Synthesis procedure of NVMP/NVMP@GN sample and the application for AZIBs cathode.

make use of the electrochemical redox reaction in both V and Mn transition metal elements for the achievement of high specific capacity. Motivated by this idea, we consider a typical NASICON,  $\text{Na}_4\text{VMn}(\text{PO}_4)_3$  (NVMP) should be an ideal candidate for high-performance Zn-ion storage. The previous study revealed superior sodium-ion storage in NVMP with a high energy density of  $\approx 380 \text{ Wh Kg}^{-1}$ .<sup>[17]</sup> However, to the best of our knowledge, there are still no studies on the Zn-ion storage behavior of NVMP in an aqueous Zn-ion battery. It is quite essential and important to understand the Zn-ion storage mechanism of NVMP to explore its application potential on aqueous batteries.

Considering most of NASICON generally suffers from poor electronic conductivity, herein, we developed graphene wrapped  $\text{Na}_4\text{VMn}(\text{PO}_4)_3$  (NVMP@GN) via a facile sol-gel method followed by a  $750^\circ\text{C}$  heat treatment in Ar gas flow (Scheme 1). Particularly, the NVMP@GN cathode exhibits an optimal specific capacity of  $254.3 \text{ mAh g}^{-1}$  at  $0.1 \text{ A g}^{-1}$  with an average discharge plateau of  $\approx 1.3 \text{ V}$ , giving a competitive energy density of  $309.7 \text{ Wh kg}^{-1}$  at a power density of  $121.6 \text{ W kg}^{-1}$ . A NASICON-based phase transition accompanied by a two-step electron transfer between  $\text{V}^{4+}/\text{V}^{3+}$  and  $\text{Mn}^{3+}/\text{Mn}^{2+}$  during the Zn-ion storage process was revealed, which makes a predominant contribution to high specific capacity and energy density. Moreover, further kinetics analysis proves the increased Zn-ion diffusion ability and electronic conductivity by graphene wrapping.

## 2. Results and Discussion

### 2.1. Rational Design of Graphene-Wrapping $\text{Na}_4\text{VMn}(\text{PO}_4)_3$

First,  $\text{Na}_4\text{VMn}(\text{PO}_4)_3$  powder sample was synthesized via a facile low-temperature sol-gel method followed by an overnight calcination treatment for crystallization improvement. In comparison, a graphene-wrapped NVMP sample was prepared with a similar method except for the addition of a spot of graphene powder during the sol-gel process (10% wt. of NVMP product) to improve the electronic conductivity of pristine NVMP. X-ray diffraction (XRD) pattern in Figure 1a indicates that all of the diffraction peaks matched well with the characteristic position in the reported trigonal phase  $\text{Na}_4\text{VMn}(\text{PO}_4)_3$  (JCPDS#98-042-3538).<sup>[18]</sup> Note that a swell ranging from  $15^\circ$  to  $25^\circ$  appears in NVMP@GN sample originating from the introduced graphene matrix (Figure 1a). A wide-range X-ray photoelectron spectroscopy (XPS) result indicates the presence of Na, V, Mn, P, and O in the as-prepared sample, while the fine spectrum for V 2p and Mn 2p confirms the valence state of  $\text{V}^{3+}$  and  $\text{Mn}^{2+}$ , respectively (Figure 1b, S1, Supporting Information).<sup>[18,19]</sup> Inductively coupled plasma atomic emission spectroscopy revealed the atom ratio Na: P: V: Mn: = 4.06: 3.01: 1.03: 0.98 of NVMP@GN sample (ICP-AES, insert in Figure 1b), which is basically consistent with the stoichiometric ratio of Na: P: V: Mn: = 4: 3: 1: 1 in  $\text{Na}_4\text{VMn}(\text{PO}_4)_3$  formula. Morphology of the samples was investigated by

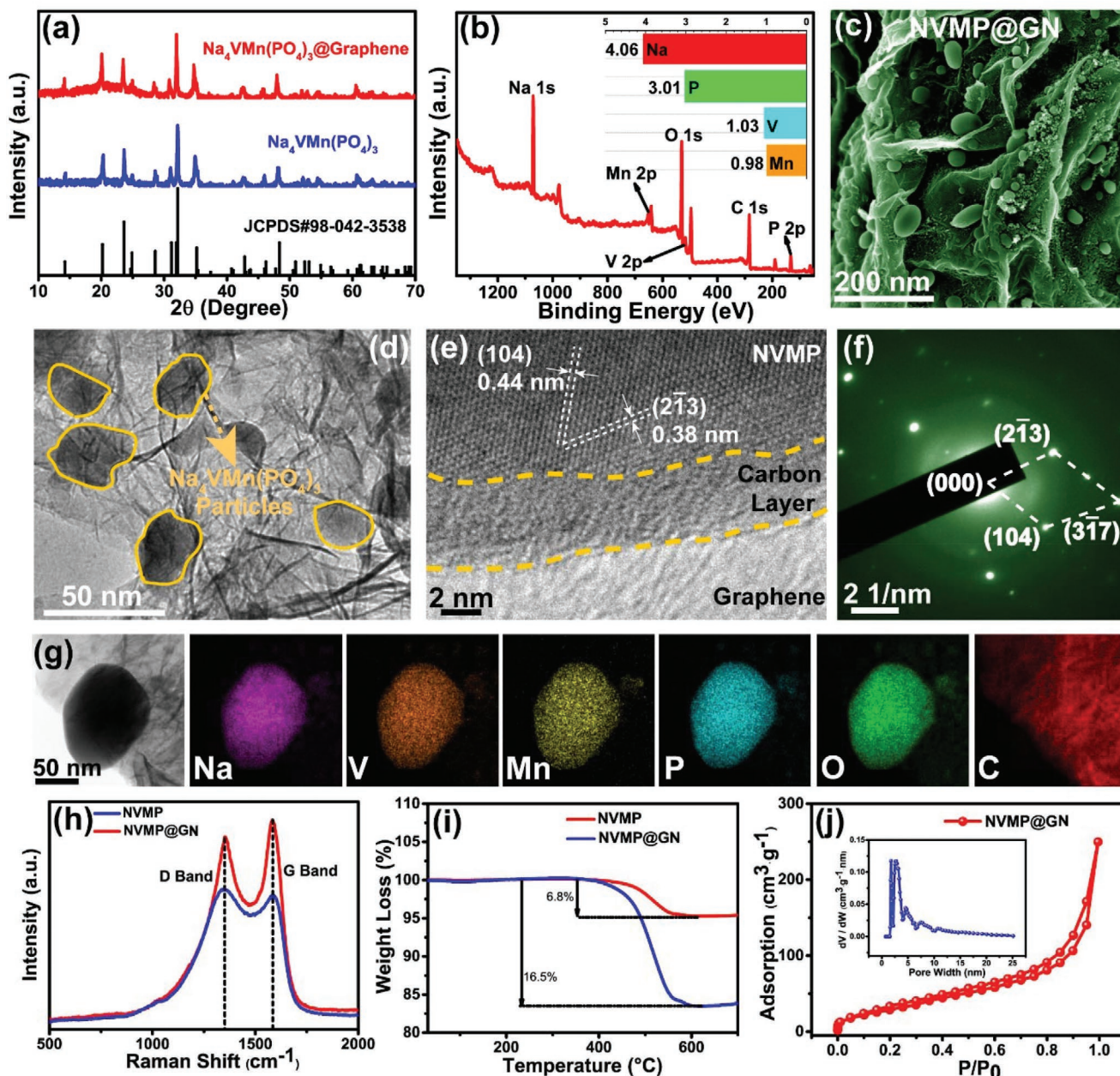


**Figure 1.** a) XRD pattern of NVMP and NVMP @ GN sample. b) Wide-range scanning result of XPS spectrum of NVMP @ GN and corresponding ICP data (insert). c) Typical SEM image of NVMP @ GN. d–g) TEM, HRTEM image, and SAED pattern of NVMP @ GN, respectively. g) EDS-mapping result of a single NVMP particle wrapped by graphene. h–j) Raman and TGA curve of NVMP and NVMP @ GN sample, respectively. j) Nitrogen adsorption-desorption curve and pore-size distribution of NVMP @ GN sample.

scanning electron microscopy (SEM) and transmission electron microscopy (TEM). By SEM observation, the NVMP@GN sample shows typical particle morphology with a feature size of  $\approx 30$  nm and a homogeneously wrapped by graphene layers (Figure 1c), while significant aggregation was observed in the pure NVMP sample (Figure S2, Supporting Information). TEM image also demonstrates the sufficient and uniform distribution of NVMP particles in graphene matrix (Figure 1d). Interestingly, a high-resolution transmission electron microscopy (HRTEM) image reveals the outer wall of

NVMP nanoparticle is homogeneously wrapped by a 5 nm thick amorphous carbon layer, which is attributed to the carbonization of citric acid during the calcination treatment.<sup>[17]</sup> Two lattice fringes were observed in the HRTEM image with a d-spacing corresponding to that of (104) and (2 $\bar{1}$ 3) planes, respectively (Figure 1e). The SAED pattern taken from an individual NVMP nanoparticle exhibited sharp indexed diffraction spots (Figure 1f).<sup>[17]</sup> Additionally, energy dispersive spectrum (EDS)-mapping focused on an individual NVMP particle also demonstrates the uniform distribution of Na, V, Mn, P, O, and

C in the NVMP@GN sample, indicating its high crystallinity with a single crystal nature (Figure 1g). The detailed surface features of the as-synthesized samples are further characterized via Raman spectroscopy. Raman spectrum of the NVMP@GN gives a remarkable hump peak  $\approx 1000\text{ cm}^{-1}$ , ascribed to the stretching vibrations mode of  $[\text{PO}_4]$  group. The intense peak located at  $\approx 1350\text{ cm}^{-1}$  (D band) and  $1590\text{ cm}^{-1}$  (G band) is attributed to  $\text{sp}^3$  (disorder-induced phonon mode) and  $\text{sp}^2$  (graphite band) carbons, respectively.<sup>[20]</sup> The calculated  $I_D/I_G$  value of the NVMP@GN sample is as low as 0.86, indicating a high content of graphitization carbon in NVMP@GN, which is attributed to the introduction of graphene (Figure 1h). Thermogravimetric analysis (TGA) curves determine the carbon content of 6.8% and 16.5% in the NVMP and NVMP@GN sample, respectively, basically consistent with the obtained Raman result (Figure 1i). Moreover, the  $\text{N}_2$  isothermal adsorption-desorption experiment gives a higher specific surface area of  $146.7\text{ m}^2\text{ g}^{-1}$  of NVMP@GN with abundant pore distribution compared to that of pristine NVMP ( $61.4\text{ m}^2\text{ g}^{-1}$ ) (Figure 1j), suggesting a remarkable

increase in surface area with the addition of graphene powder, which is usually very favorable for fast ion transport and storage for energy applications.

## 2.2. Zn-ion Battery Performance

To evaluate the Zn-ion storage performance of the as-constructed NVMP @ GN, CR-2032 coin cells were assembled, employing NVMP @ GN as the cathode active material, zinc foil as an anode (counter electrode), respectively. The average mass loading and coating thickness of the slurry on the substrate is  $\approx 2\text{ mg cm}^{-2}$  and  $150\text{ }\mu\text{m}$ , respectively. Considering that adequate  $\text{MnSO}_4$  was regarded as crucial electrolyte additive for the suppression of Mn dissolution that occurred in traditional Mn-based compounds,  $2\text{ M Zn}(\text{SO}_4)_2/0.2\text{ M MnSO}_4$  was used as the aqueous electrolyte.<sup>[21,22]</sup> Figure 2a shows the representative cyclic voltammetry (CV) curve of the NVMP cathode-based battery at the scan rate of  $0.1\text{ mV s}^{-1}$  in the voltage range

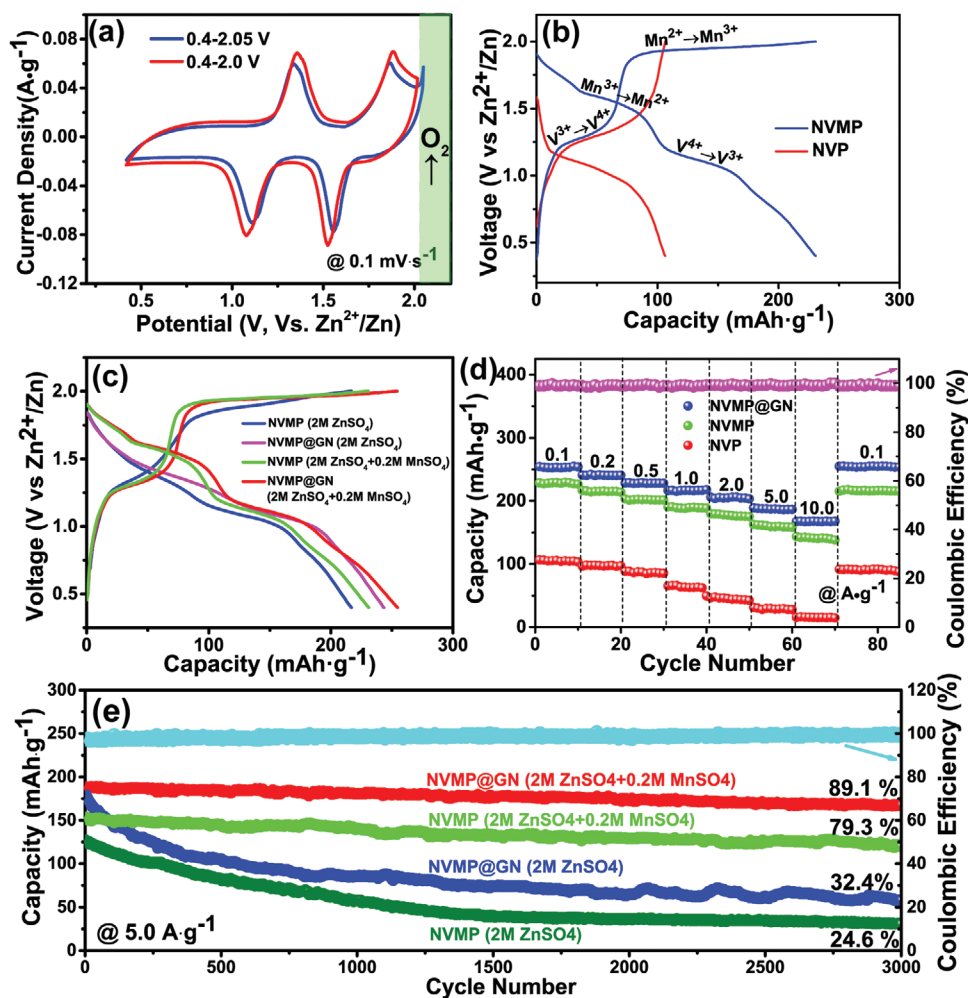


**Figure 2.** a) CV curve of  $\text{Zn} // (2\text{ M ZnSO}_4/0.2\text{ M MnSO}_4) // \text{NVMP}$  battery in the voltage range between 0.4–2.0 V and 0.4–2.05 V, respectively. b) GCD curve of NVMP and NVP based battery at a current density of  $0.1\text{ A g}^{-1}$ , respectively. c) GCD curves of  $\text{Zn} // \text{NVMP}$  battery,  $\text{Zn} // \text{NVMP @ GN}$  battery with two different electrolytes ( $2\text{ M ZnSO}_4$ ,  $2\text{ M ZnSO}_4/0.2\text{ M MnSO}_4$ ). d) Rate-performance of NVMP @ GN cathode ( $2\text{ M ZnSO}_4/0.2\text{ M MnSO}_4$ ). e) Long-term cycle performance of  $\text{Zn} // \text{NVMP @ GN}$  battery ( $2\text{ M ZnSO}_4/0.2\text{ M MnSO}_4$ ).

from 0.4–2.0 V respectively. The CV curves exhibit noteworthy two-step electron transfer accompanied by two pairs of redox peaks located at  $\approx 1.3/1.1$  V and  $1.85/1.55$  V, which is ascribed to  $V^{4+}/V^{3+}$  and  $Mn^{3+}/Mn^{2+}$  redox couple, respectively. However, when the scanning voltage upper limit is 2.05 V, a distinct side reaction is observed in the positive scanning between 2.0–2.05 V, which should be attributed to oxygen generated in high-voltage section.<sup>[23]</sup> This side reaction is also detected in the corresponding galvanostatic charge-discharge (GCD) curve when the battery is charged to 2.05 V (Figure S3, Supporting Information). The discharge/charge plateau voltage in the GCD curve is mostly accordant with the redox peak voltage in CV curve. Known that proton insertion is very common in aqueous batteries. However, when we compare the CV curves of the battery tested in aqueous electrolyte and acetonitrile electrolyte respectively (Figure S4, Supporting Information), we found these two CV curves show almost the same shape with no changes in the location of redox peaks. Note that the area of the CV loop in acetonitrile is obviously smaller than that of in aqueous electrolyte, which should be attributed to the more sluggish zinc-ion diffusion kinetics in acetonitrile compared with that in aqueous electrolyte. Accordingly, the same CV shapes verify the absence of proton insertion/exaction in our cathode. In view of the obtained CV curves, it is rational that the charge-discharge voltage range of our NVMP cathode should be controlled at less than 2.0 V. GCD curve of NVMP-based battery displays a specific capacity of  $230.7 \text{ mAh g}^{-1}$  with two distinct discharge plateau at 1.55 V and 1.1 V ( $Mn^{3+}/Mn^{2+}$  and  $V^{4+}/V^{3+}$ ) under the current density of  $0.1 \text{ A g}^{-1}$ , while the GCD curve of a  $Na_3V_2(PO_4)_3$  (NVP)-based battery shows a much lower discharge capacity of  $106.5 \text{ mAh g}^{-1}$  with a single discharge plateau at 1.1 V ( $V^{4+}/V^{3+}$ ) (Figure 2b). This result demonstrates that the capacity and discharge voltage has been remarkably enhanced by the introduction of Mn in NVP structure. GCD curves obtained in the initial 10 cycles show apparently diverse charge curve in the 1<sup>st</sup> cycle, which should be related to a pioneer extraction of sodium-ion in NVMP framework. Similar situation has been observed in the  $Na_3V_2(PO_4)_3$  cathode in zinc-ion battery reported previously.<sup>[11]</sup> Note that the charge-discharge curves are subsequently stabilized from the 2<sup>nd</sup> cycle, implying reversible Zn-ion storage reaction in the successive cycles (Figure S5, Supporting Information). To demonstrate the positive contribution of graphene wrapping, contrastive GCD test was also processed employed NVMP@GN cathode with the use of varied electrolyte. Apparently, NVMP@GN composite cathode exhibits superior capability in both 2M  $ZnSO_4$  ( $243.7 \text{ mAh g}^{-1}$ ) and 2M  $ZnSO_4/0.2 \text{ M MnSO}_4$  ( $254.4 \text{ mAh g}^{-1}$ ) electrolyte, while the pure NVMP possesses a lower specific capacity of  $216.8 \text{ mAh g}^{-1}$  and  $230.7 \text{ mAh g}^{-1}$ , respectively, which should be attributed to conductivity enhancement by graphene wrapping. Especially, the GCD curves with  $MnSO_4$  addition in electrolyte exhibit a more conspicuous discharge plateau at  $\approx 1.55$  V, implying effective inhibition of Mn-dissolution contributed by Mn-salt addition (Figure 2c).

As for rate performance, the graphene wrapped NVMP @ GN sample in 2M  $ZnSO_4/0.2 \text{ M MnSO}_4$  electrolyte gives a competitive reversible capacity of  $163.5 \text{ mAh g}^{-1}$  with a steady GCD curve even at a high current density of  $10.0 \text{ mAh g}^{-1}$ , superior to that of the pure NVMP sample ( $143.5 \text{ mAh g}^{-1}$ ). In contrast,

the un-doped V-based NVP sample shows a significantly lower rate capability of just  $15.6 \text{ mAh g}^{-1}$  at the same current density. (Figure 2d, S6, Supporting Information). Remarkably, the as-obtained rate capability of our NVMP@GN cathode exceeds most conventional materials for AZIB such as V-based compounds ( $Zn_3V_2O_7(OH)_2 \cdot 2H_2O$ ,<sup>[24]</sup>  $Na_3V_2(PO_4)_3$ <sup>[11]</sup>), Mn-based oxides ( $\alpha\text{-MnO}_2$ ,<sup>[25]</sup>  $Mn_2O_3$ ,<sup>[26]</sup>  $Mn_3O_4$ ,<sup>[27]</sup>) and also  $Co_3O_4$ ,<sup>[28]</sup> (Figure S7, Supporting Information). Furthermore, long-term cycle test at the current density of  $5.0 \text{ A g}^{-1}$  reflects a severe capacity decay of pure NVMP (24.6% retention) and NVMP@GN (32.4% retention) in 2M  $ZnSO_4$  electrolyte after 3000 cycles, significantly inferior to that in 2M  $ZnSO_4/0.2 \text{ M MnSO}_4$  mixed electrolyte (NVMP: 79.3% retention, NVMP@GN: 89.1% retention) (Figure 2e). The first-cycle coulomb efficiency of these batteries is 84.8%, 86.1%, 90.9%, and 93.4%, respectively. Therefore, the resulted rapid capacity decay caused by Mn-dissolution is significantly suppressed via Mn-salt addition in the aqueous electrolyte. Recent works clarified that the electrolyte formulation has a remarkable influence on the cycling stability.<sup>[29–31]</sup> Considering that some electrolyte additives may undergo the reduction process and deposit on the Zn anode with possible capacity contribution, we performed a Mn 2p XPS characterization of the Zn anode after 100 and 300 cycles. No apparent signal peak can be observed in such a Mn 2p core-level spectrum (Figure S8, Supporting Information). Hence, it can be confirmed that the  $MnSO_4$  additive is chemically stable during the charge-discharge procedure. The SEM/TEM characterization of the active material after 100–300 long-term cycles indicates the initial morphology and phase structure can be well maintained, demonstrating the excellent electrochemical stability of our NVMP@GN (Figure S9, Supporting Information). We found the *d*-spacing of NVMP (104) after 300 cycles is 0.38 nm, which is slightly smaller than the initial value (0.44 nm). This slight decrease in lattice spacing should be attributed to the partial substitution of  $Na^+$  by  $Zn^{2+}$  after long-term charge/discharge cycles. Note that the radius of  $Zn^{2+}$  (0.74 Å) is a little smaller than that of  $Na^+$  (1.02 Å) while the surface charge density of  $Zn^{2+}$  is higher than that of  $Na^+$ , thus leading to the lattice contraction after  $Zn^{2+}$  insertion.

To have an intuitive comparison of the performance advantage between our NVMP@GN cathode and other cathode materials for AZIBs, a discharge plateau versus specific capacity diagram including our NVMP@GN, Mn-based compounds,<sup>[26,32,33]</sup> V-based oxides,<sup>[24,34–43]</sup> Prussian Blue analogs,<sup>[44–46]</sup> polyanionic compounds,<sup>[10–12,47–49]</sup> chalcogenides<sup>[28,50–52]</sup> and some organics<sup>[53–57]</sup> is shown as Figure 3a. Detailed data (specific capacity, voltage plateau) of these contrastive cathode materials is listed in Table S1 (Supporting Information). Especially, the performance of our V-Mn incorporated NVMP@GN cathode is dramatically superior to that of V-based NVP cathode.<sup>[11]</sup> Benefiting from the overall performance merits on discharge voltage plateau, high specific capacity and prominent rate-capability, our NVMP @ GN cathode exhibits a high energy density of  $309.7 \text{ Wh kg}^{-1}$  at a power density of  $121.6 \text{ W kg}^{-1}$  suppressing most of the popular cathode materials for AZIB recently reported involving  $V_3O_7 \cdot nH_2O$ ,<sup>[36]</sup>  $\alpha\text{-MnO}_2$ ,<sup>[58]</sup>  $ZnMn_{1.86}O_4$ ,<sup>[32]</sup>  $CuHCF$ <sup>[59]</sup>  $ZnHCF$ <sup>[44]</sup> and the un-doped V-based  $Na_3V_2(PO_4)_3$  sample ( $107.7 \text{ Wh kg}^{-1}$  @  $101.3 \text{ W kg}^{-1}$ , as shown in Ragone plot in Figure 3b).

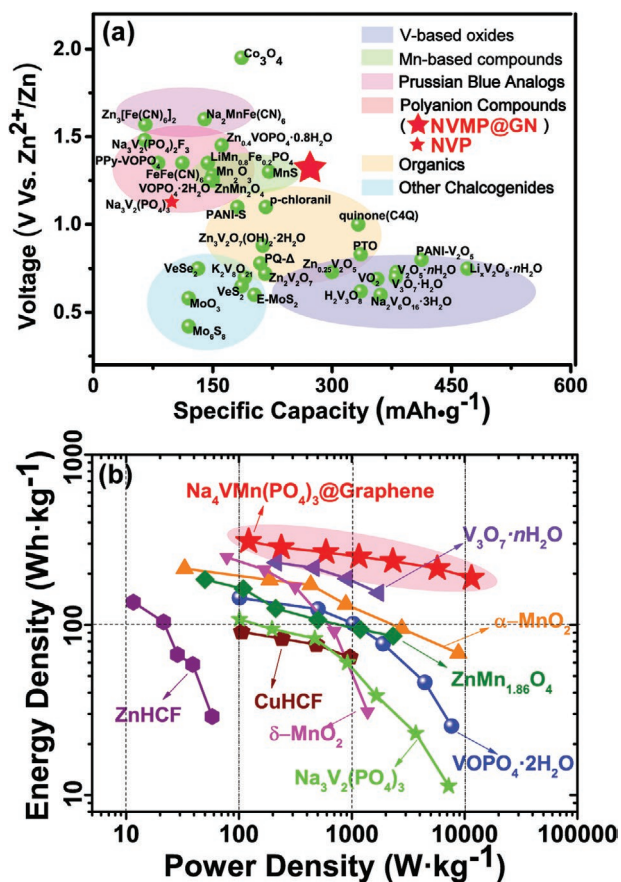


**Figure 3.** a) Discharge voltage plateau versus specific capacity diagram. b) Ragone plot of our NVMP @ GN, un-doped NVP, and other conventional cathodes, respectively.

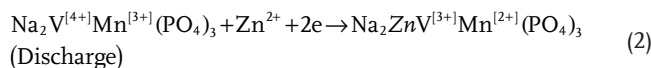
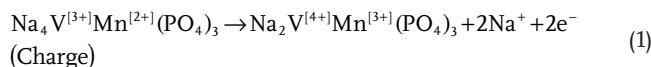
### 2.3. Zn-ion Storage Mechanism and Transport Kinetics

More attention has been paid to understand its energy storage mechanism. Ex situ XRD and XPS characterizations were conducted, respectively. **Figure 4a** displays a typical GCD curve and relative sampling points in the 1<sup>st</sup> cycle for ex situ observation. As can be seen in the corresponding XRD patterns, all the dominant diffraction peaks shifted to a higher  $2\theta$  degree along with the initial charging procedure to 2.0 V, while the corresponding peaks gradually turned back to the lower degree when the battery is discharged to 0.4 V. Notably, the final  $2\theta$  degree of these peaks is a little bit higher than those of the pristine  $\text{Na}_4\text{VMn}(\text{PO}_4)_3$  phase. Especially, no peaks belonging to other phases appeared during the continuous charge and discharge process (Figure 4b). The ex situ XRD characterization gives a feasible sodium-ion extraction/Zn-ion insertion mechanism with the maintenance of the general NASICON framework during the first charge-discharge procedure. Additionally, ex situ XPS results demonstrate a featured binding energy (BE) of 641.3 eV and 516.2 eV of Mn 2p and V 2p characteristic peak, respectively, implying the existence of  $\text{Mn}^{2+}$  and  $\text{V}^{3+}$  in the pristine  $\text{Na}_4\text{VMn}(\text{PO}_4)_3$  phase. When the battery was charged to the high-voltage of 2.0 V, the characteristic peak of Mn 2p and V 2p severally shifted to a higher BE of 642eV and 516.8 eV, in

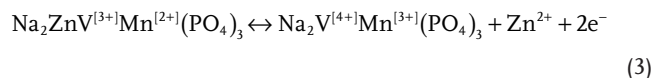
consistent with a high oxidation state of  $\text{Mn}^{3+}$  and  $\text{V}^{4+}$ . With the fully discharged stage at 0.4 V, the spectrum of the two transition elements was converted back to the initial state, respectively, proving the recovered oxidation state of  $\text{Mn}^{2+}$  and  $\text{V}^{3+}$  after a complete charge/discharge cycle.<sup>[17,60]</sup> Moreover, Na 1s core-level spectrum shows a dramatically decreased intensity of its characteristic peak at the fully charged (2.0 V) state, while the peak density remains basically unchanged at the followed fully discharged (0.4 V) state (Figure 4d). Meanwhile, spectrum of Zn 2p reflects significant enhancement of the featured peak after 1<sup>st</sup> discharged process (Figure 4e).

According to these ex situ characterizations, the Zn-ion storage mechanism in the  $\text{Na}_4\text{VMn}(\text{PO}_4)_3$  phase can be thus summarized as follows: sodium-ion is partially extraction from the  $\text{Na}_4\text{VMn}(\text{PO}_4)_3$  framework to form a  $\text{Na}_2\text{VMn}(\text{PO}_4)_3$  phase during the initial charge state, which is confirmed by oxidation of  $\text{V}^{3+}$  to  $\text{V}^{4+}$  and  $\text{Mn}^{2+}$  to  $\text{Mn}^{3+}$  revealed by XPS result and also the slight shift into a larger diffraction degree as shown in XRD pattern. Subsequently, Zn-ion insertion appeared in the followed discharge process to form a  $\text{Na}_2\text{ZnVMn}(\text{PO}_4)_3$  phase with well remaining the as-established NASICON structure. A two-step electron transfer occurred between  $\text{Mn}^{2+}/\text{Mn}^{3+}$  and  $\text{V}^{3+}/\text{V}^{4+}$  is therefore observed, respectively. In the subsequent cycles, reversible Zn-ion exaction/insertion will continuously proceed without sodium-ion participation (Figure 4f). In contrast, electron transfer in the NVP cathode only occurs in V atoms with a rather limited capacity contribution.<sup>[11]</sup> The corresponding electrochemistry reaction equation is then illustrated as follows:

In the first cycle:



In the subsequent cycles:



Detailed electrochemical experiment analysis was successively conducted to clarify the internal kinetics behavior behind the competitive Zn-ion storage performance of our NVMP cathode. Cyclic voltammetry (CV) curves of the Zn//NVMP battery with varied scan rate give a vital dependence of the peak current density and scan rate to clarify the capacity contribution type for Zn-ion storage in NVMP cathode (**Figure 5a**). In terms of the certificated principle, the peak current density and the corresponding scan rate in a specialized CV curve obey the following relationship:<sup>[61,62]</sup>

$$i = av^b \quad (4)$$

where  $a$  and  $b$  are variable values due to the capacity contribution type. A  $b$  value of 0.5 implies a semi-infinite diffusion mechanism, while a  $b$  value of 1.0 indicates predominant capacitive behavior. With regard to our NVMP@GN cathode, the  $b$

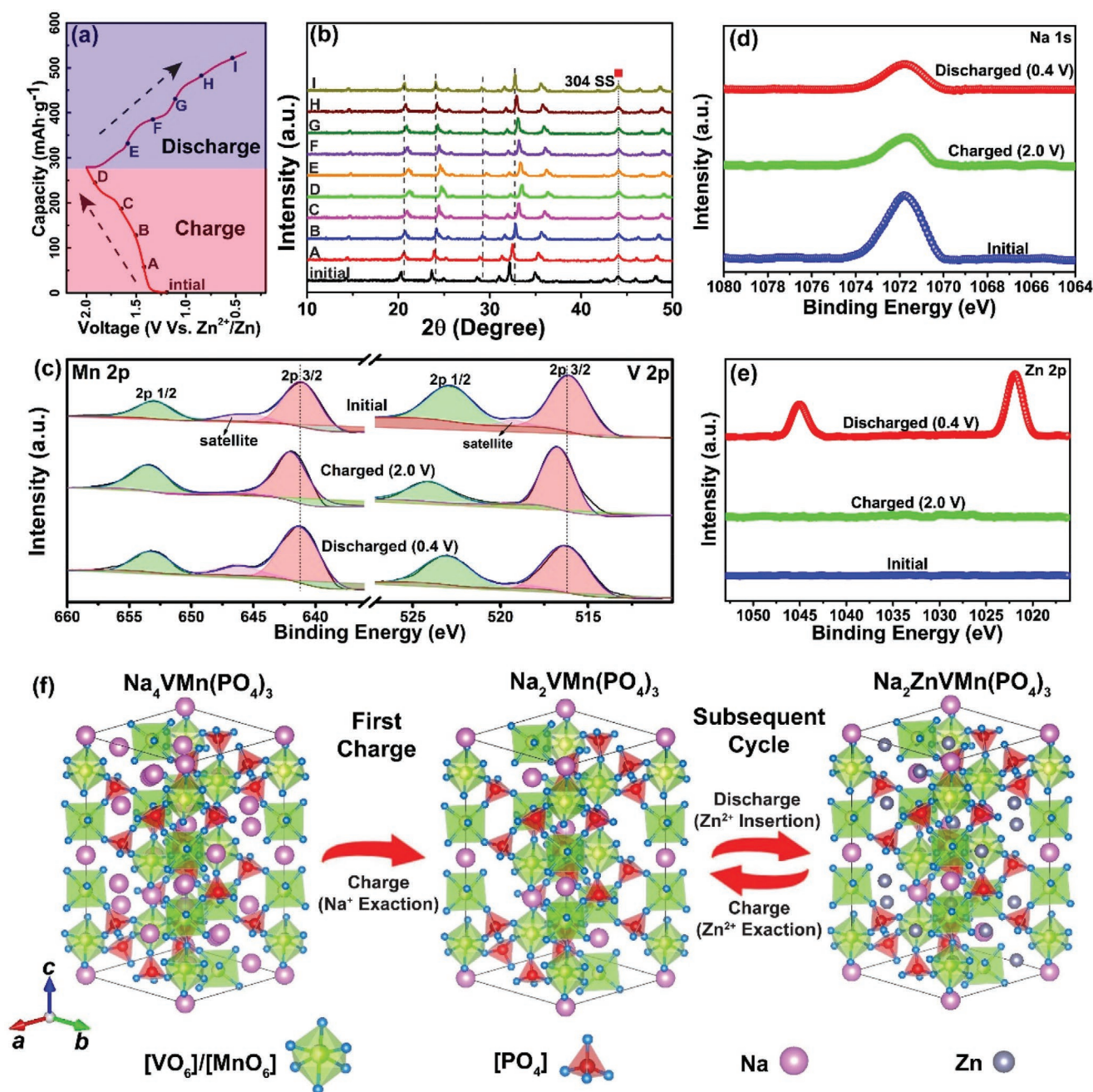


**Figure 4.** a) GCD curve and b) the corresponding ex situ XRD patterns of NVMP cathode in a complete charge-discharge procedure, respectively. c–e) Ex situ XPS spectrum for Mn, V, Na, and Zn element of the NVMP cathode sampled at different charge-discharge state (initial, fully charged, and fully discharged), respectively. f) Schematic illustration of the Zn-ion storage mechanism in NVMP.

value of 0.78, 0.79, 0.80, and 0.79 can be derived for the peak A to peak D of the four primary peaks, respectively, indicating capacitive-effect is the predominant contribution for Zn-ion storage (Figure S10, Supporting Information). A capacitive contribution of 58.7%, 61.4%, 65.8%, 68.2%, and 70.9% at the scan rate of 0.1, 0.2, 0.5, 0.8 and 1.0 mV s<sup>-1</sup> is calculated, respectively (Figure 5b). A typical CV curve containing both the capacitive (58.7%) and diffusion contribution (41.3%) is also shown in Figure 5c.

Furthermore, the galvanostatic intermittent titration technique (GITT) technique was likewise employed to study the property of Zn-ion diffusion in the cathode (Figure 5d). Strikingly, an ultrahigh Zn-ion diffusion coefficient of  $4.1 \times 10^{-8}$  cm<sup>2</sup> s<sup>-1</sup> was observed in NVMP@GN cathode (2M ZnSO<sub>4</sub>+0.2 M MnSO<sub>4</sub>), surpassing that of NVMP@GN cathode in 2M ZnSO<sub>4</sub> ( $5.5 \times 10^{-9}$  cm<sup>2</sup> s<sup>-1</sup>) and the NVMP cathode in 2M ZnSO<sub>4</sub> ( $2.7 \times 10^{-10}$  cm<sup>2</sup> s<sup>-1</sup>), in consistent with the optimal performance of NVMP@GN cathode with mixed electrolyte addition.

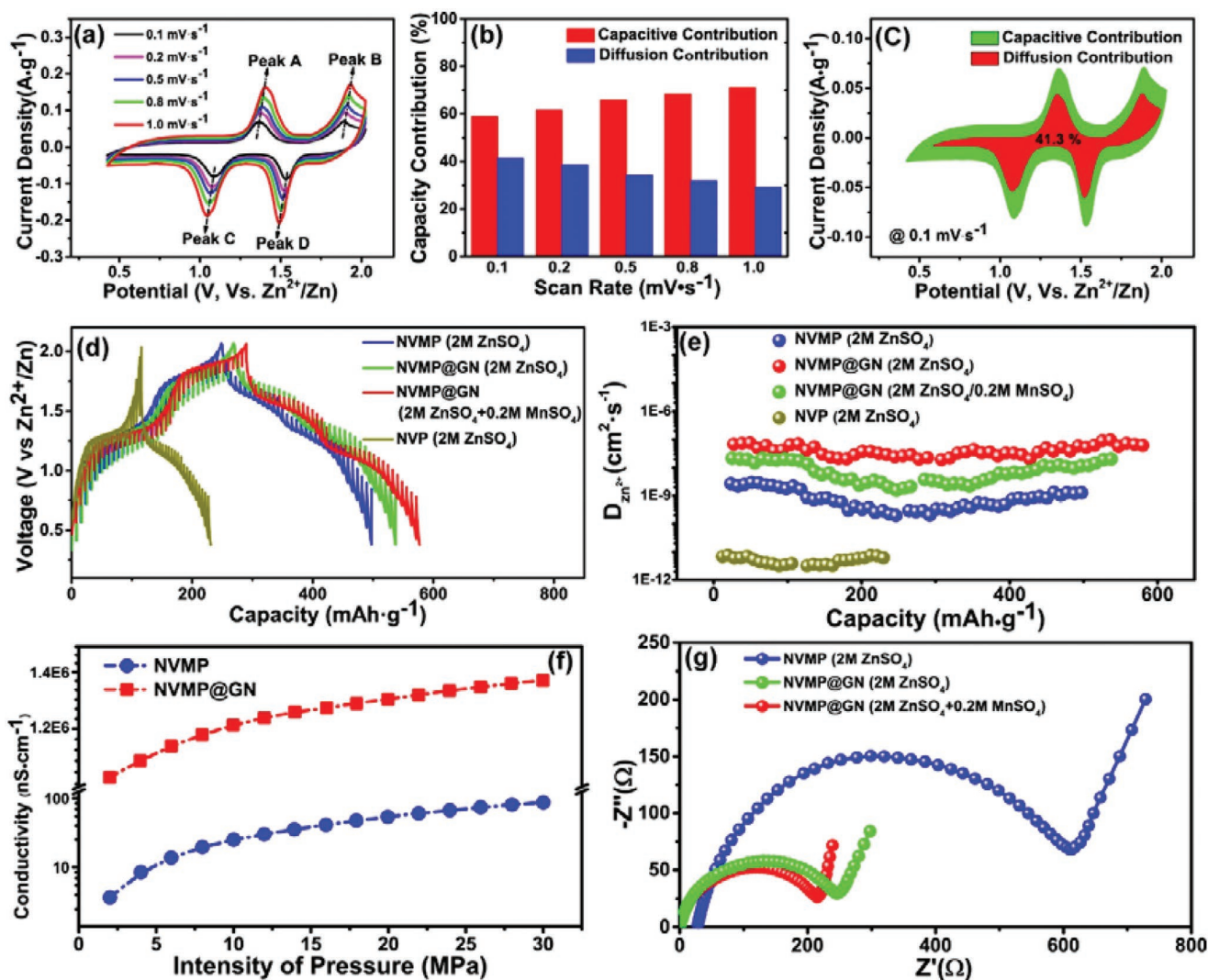


**Figure 5.** a) CV curves of Zn//NVMP battery at different scan rate, respectively. b) Capacitive and diffusion contribution bar graph calculated from the dependence of peak current density and the scan rate. c) A typical CV curve containing the schematic of capacitive and diffusion contribution of NVMP cathode. d) GITT curve and e) the calculated diffusion coefficient of NVMP and NVMP @ GN cathode with different electrolyte (2M ZnSO<sub>4</sub>, 2M ZnSO<sub>4</sub> + 0.2 M MnSO<sub>4</sub>), respectively. f) Four-probe conductivity test under different pressure. g) Nyquist plot of NVMP and NVMP@GN cathode in the different electrolyte.

Emphatically, in addition to the diffusion ability improvement realized by conductive graphene wrapping, it's arresting that superior diffusion condition is achieved for high-voltage Mn<sup>3+</sup>/Mn<sup>2+</sup> plateau with MnSO<sub>4</sub> additive, demonstrating effective stabilization of Mn in NVMP framework with Mn-electrolyte addition. In contrast, the NVP cathode only had an apparently lower diffusion coefficient of  $4.8 \times 10^{-12} \text{ cm}^2 \text{ s}^{-1}$ , clarifying effective kinetics improvement in Mn-doped NVMP cathode. (Figure 5e). On the other hand, the corresponding impedance study further reveals the conductivity improvement with graphene wrapping and MnSO<sub>4</sub> addition. Four-probe conductivity experiment exhibits a five orders of magnitude higher electronic conductivity of the NVMP@GN sample when contrast to the pure NVMP sample with quite poor intrinsic electronic conductivity due to the achievement of graphene wrapping (Figure 5f). Meanwhile, the typical Nyquist plot shows observably decreased

series resistance and charge transfer resistance of the graphene wrapped sample, while the plot of the cathode in a mixed electrolyte (MnSO<sub>4</sub> addition) also displayed a lower Warburg diffusion impedance with a bigger slope in the low-frequency range, proving signally enhanced structure stability and diffusion ability with MnSO<sub>4</sub> addition (Figure 5g).

#### 2.4. Flexible Electronic Applications

With the purpose to identify the application potential on flexible and wearable electronics, a soft package battery employing slurry-coated NVMP@GN@ carbon fiber cloth (CFC) as cathode, 0.5 M Zn(ClO<sub>4</sub>)<sub>2</sub> @ polyvinyl alcohol (PVA) as quasi-solid-state hydrogel electrolyte and zinc foil as both anode and counter electrode was thereupon assembled (Figure 6a).

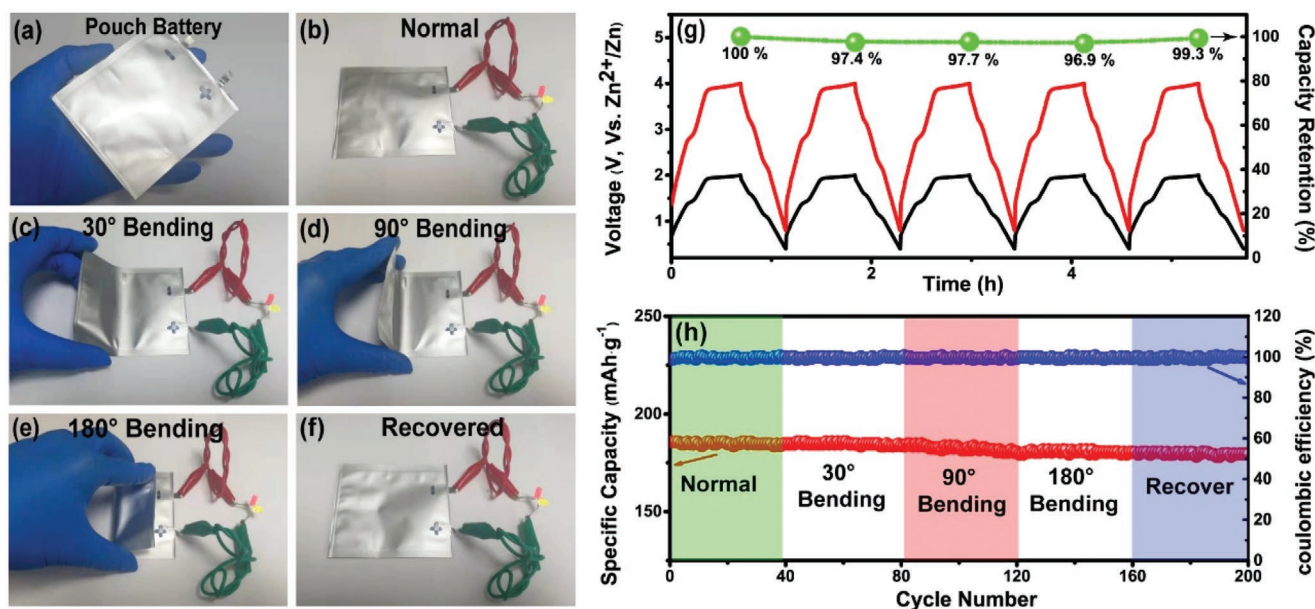


**Figure 6.** a) Soft-packed Zn/0.5 M Zn(ClO<sub>4</sub>)<sub>2</sub>/NVMP @ GN battery and b–f) a LED driving test under varied bending angle, respectively. g) GCD curves of a Zn//NVMP @ GN pouch battery and two batteries in series under various bending state (normal, 30°, 90°, 180°, and recovered), respectively. h) Long-term cycle test of the as-fabricated pouch battery at 1.0 A g<sup>-1</sup> with various bending angle.

Expressly, Zn(ClO<sub>4</sub>)<sub>2</sub> was used here rather than commonly used ZnSO<sub>4</sub> due to the higher solubility of Zn(ClO<sub>4</sub>)<sub>2</sub> in PVA hydrogel.<sup>[12]</sup> Figure 6b–f exhibits the fully charged soft package battery driving a group of light-emitting diode (LED) steadily under varied bending state (normal, 30°, 90°, 180°, and recovered). To comprehensively study the electrochemical performance of our flexible battery, GCD test of the assembled battery as well as two batteries in series under corresponding bending test shows stable charge–discharge curve and satisfied capacity retention (capacity decay less than 3%) at varied bending states (Figure 6g), respectively, demonstrating excellent flexibility and promising wearable potential of our soft package battery. A subsequent cyclic charge–discharge test (@ 1.0 A g<sup>-1</sup>) likewise investigated the excellent lifespan of the battery with impressive flexibility (96.7% retention after 200 cycles) (Figure 6h).

### 3. Conclusion

In summary, we incorporated V and Mn elements simultaneously into the NASICON host to make use of the electrochemical redox reaction in both V and Mn transition metal elements for aqueous Zn-ion storage. A significant increase in both capacity and working voltage has been observed after Mn doping into Na<sub>3</sub>V<sub>2</sub>(PO<sub>4</sub>)<sub>3</sub> to form Na<sub>4</sub>VMn(PO<sub>4</sub>)<sub>3</sub>. The latter exhibits a high capacity of 230.7 mAh g<sup>-1</sup> with a discharge plateau at 1.55–1.1 V, while the former just shows a much lower discharge capacity of 106.5 mAh g<sup>-1</sup> with a working plateau at 1.1 V. Taking advantage of the merits on both high capacity and high voltage, our Na<sub>4</sub>VMn(PO<sub>4</sub>)<sub>3</sub>@Graphene cathode delivers an optimal energy density of 309.7 Wh kg<sup>-1</sup> with very stable cycle performance (89.1% capacity retention after 3000 cycles at 5.0 A g<sup>-1</sup>). Transport kinetics studies also confirm an ultrahigh

Zn-ion diffusion coefficient of 4.1 × 10<sup>-8</sup> cm<sup>2</sup> s<sup>-1</sup>. Our work developed NASICON-typed Na<sub>4</sub>VMn(PO<sub>4</sub>)<sub>3</sub> as a promising candidate for AZIBs cathode. It also provides a promising prospect for the rational design of hetero-atom doping (such as Cu, Co, Fe, F...) phase to realize further performance enhancement.

### 4. Experimental Section

**Material Synthesis:** Na<sub>4</sub>VMn(PO<sub>4</sub>)<sub>3</sub> (NVMP) particle was synthesized via a facile sol-gel method combined with an overnight calcination process. To be specific, 0.273 g V<sub>2</sub>O<sub>5</sub> (1.5 mmol), 0.735 g of Mn(CH<sub>3</sub>COO)<sub>2</sub>·4H<sub>2</sub>O (3 mmol), and 0.636 g of Na<sub>2</sub>CO<sub>3</sub> (6 mmol) of 1.035 g were successively added into 50 mL of deionized (DI) water under continuous magnetic stirring at 80 °C to form a uniform transparent solution. Then, 0.865 g of citric acid (4.5 mmol) was added into the solution as both a carbon source and a reducing agent to reduce V<sup>5+</sup> to V<sup>4+</sup>. The mixed solution was kept stirring for 20 min, followed by the slow addition of 1.035 g of NH<sub>4</sub>H<sub>2</sub>PO<sub>4</sub> (9 mmol) to form the primary NVMP sol. The mixed aqueous system was kept heating and stirring for another 2 h to evaporate excess water to obtain a wet gel. After a further drying process at 60 °C in the oven, the dried gel was grinded carefully and calcinated at 750 °C for 9 h under the protection of argon flow in a tube furnace to acquire the well-crystallized NVMP particles.<sup>[17]</sup> Graphene wrapped Na<sub>4</sub>VMn(PO<sub>4</sub>)<sub>3</sub> (NVMP@GN) sample was synthesized using a similar method except for the addition of 10 wt.% of graphene in the reaction mixture.

**Material Characterization:** Scanning electron microscopy (SEM, Phenom Pro X), high-resolution transmission electron microscopy (TEM, Philips CM 200 FEG Field Emission Microscope), and X-ray diffraction (XRD, Bruker D8-A25 diffractometer using Cu Kα radiation (λ = 1.5406 Å)) were respectively employed for the morphology and primary phase characterization of the as-synthesized samples. Corresponding selected electron diffraction (SAED) and energy-dispersive spectrum (EDS-mapping) tests were carried out, accompanied by the TEM measurement to characterize the information of featured lattice and element distribution. Further characterization of the chemical bonding and microscopic conditions was revealed

by the X-ray photoelectron spectrum (XPS, PHI 5000C EACA), Raman spectrum (RENISHAW inVia), thermogravimetric analysis (TGA, SDT Q600), and Brunner-Emmet-Teller method (BET) specific surface area test (Quadrachrome), respectively. An electronic conductivity test was carried out on a four-probe conductivity tester (ST2253y).

**Electrochemical Measurement:** CR-2032 coin cells were assembled using as-synthesized NVMP or NVMP@GN as cathode, 2M pure ZnSO<sub>4</sub> or 2M ZnSO<sub>4</sub>/0.2 M MnSO<sub>4</sub> mixed solution as an electrolyte, and zinc foil as an anode as well as counter, respectively. Cathode slurry was prepared by mixing as-prepared samples, acetylene black and polyvinylidene fluoride (PVDF) based on a mass ratio of 7:2:1 with the addition of 1-methyl-2-pyrrolidinone (NMP). The uniform slurry was then coated onto a piece of 304 stainless steel (304ss) foil and dried in a vacuum oven at 110 °C for 10 h. The average mass loading and coating thickness of the slurry on the substrate was ≈2 mg cm<sup>-2</sup> and 150 μm, respectively. The slurry-coated foil was cut into Φ15 mm electrode as a cathode, while the same size zinc foil washed with ethanol and glass fiber membrane was employed as an anode and separator, respectively. The AZIBs were assembled in the air with the necessary relevant components. LAND battery test system (CT2001A) was used to study the Zn-ion storage performance. Cyclic voltammetry (CV) test at different scan rate and electrochemical impedance spectrum (EIS) with varied frequencies ranging from 100 kHz to 0.01 Hz and an applied alternating voltage (AC) of 5 mV was performed on an electrochemical workstation (CHI660E) to evaluate the kinetics feature, respectively. The galvanostatic intermittent titration technique (GITT) was performed under a unique GCD mode, in which a working period containing two-stage: a charge/discharge process last for 15 min at 0.03 A g<sup>-1</sup> and followed a pause time for 15 min.

**Fabrication of the Pouch Battery:** The pouch battery was fabricated using the aforementioned slurry-coated carbon fiber cloth (CFC) as the cathode (mass loading: 2 mg cm<sup>-2</sup>), CFC with a layer of zinc electrodeposited coating as the anode, a piece of filter paper as the separator, and 2M Zn(ClO<sub>4</sub>)<sub>2</sub> @ polyvinyl alcohol (PVA) as the electrolyte. The electrolyte was prepared by adding 3 g of PVA to 30 mL of 2M Zn(ClO<sub>4</sub>)<sub>2</sub> aqueous solution little by little with continuous stirring, followed by oil bath treatment at 80 °C for 2 h and gathering the gel-like sample when the system was cooled down to the room temperature. The electrochemical deposition of the zinc layer on the CFC was carried out on CHI660E using a potentiostatic model at -0.7 V (vs Zn<sup>2+</sup>/Zn) for 2000 s. The fully assembled pouch battery was finally sealed with aluminum foil as a sandwich structure.

**Calculation Methods:** The calculation method for the capacity contribution of the cathodes was based on the following equation:

$$I_p = C_1 \nu + C_2 \nu^2 \quad (5)$$

where  $I_p$  (A g<sup>-1</sup>) is the peak current density at different scan rate,  $\nu$  (mV s<sup>-1</sup>) is the specific scan rate,  $C_1$  and  $C_2$  are the corresponding constant factors of the capacity contribution of surface pseudocapacitive effect and battery-type effect, respectively.

After a necessary deformation of the equation, a particular contribution of capacitive/battery type can be solved in term of the following equation:

$$\frac{I_p}{\nu^2} = C_1 \nu^{\frac{1}{2}} + C_2 \quad (6)$$

The specific energy density (Wh kg<sup>-1</sup>) and average specific power density (W kg<sup>-1</sup>) of the batteries is calculated in terms of the following equations:

$$E_s = \int_{V_0}^{V_1} C_s (V) \quad (7)$$

$$P_s = \frac{E_s}{t} \quad (8)$$

Where  $E_s$  is the calculated specific energy density (Wh kg<sup>-1</sup>),  $P_s$  is the average specific power density (W kg<sup>-1</sup>);  $C_s$  (mAh g<sup>-1</sup>) is the specific capacity of the battery,  $V_0$  and  $V_1$  is the voltage lower limit and voltage upper limit of discharge procedure, respectively, and  $t$  is the discharge time (h). All the parameters calculated were based on the mass loading of the active materials (NVMP and NVMP@GN).

Diffusion coefficient ( $D_{Zn^{2+}}$ ) of Zn-ion can be experimentally calculated by GITT method in terms of the following equation:<sup>[42]</sup>

$$D = \frac{4}{\pi \tau} L^2 \left( \frac{\Delta E_s}{\Delta E_t} \right)^2 \quad (9)$$

Where  $D$  is the diffusion coefficient of Zn-ion,  $\tau$  is the relaxation time of the current pulse,  $L$  is diffusion length which is approximate to the thickness of coated slurry,  $\Delta E_s$  and  $\Delta E_t$  is the voltage change produced by current pulse and the galvanostatic charge/discharge, respectively.

## Supporting Information

Supporting Information is available from the Wiley Online Library or from the author.

## Acknowledgements

This work was financially supported by the Natural Science Foundation of Jiangsu Province (Grants No. BK20211516), the National Natural Science Foundation of China (52171203, 51872051), National Key Research and Development Program of China (Grant No. 2021YFB2400400), the State Key Laboratory of New Ceramic and Fine Processing Tsinghua University (No. KF202102), and the Fundamental Research Funds for the Central Universities (2242022R10090).

## Conflict of Interest

The authors declare no conflict of interest.

## Data Availability Statement

The data that support the findings of this study are available from the corresponding author upon reasonable request.

## Keywords

aqueous Zn-ion batteries, high energy density, multiple-electron transfer, Na<sub>4</sub>VMn(PO<sub>4</sub>)<sub>3</sub>, NASICON

Received: February 24, 2022

Revised: April 6, 2022

Published online: April 23, 2022

- [1] J. B. Goodenough, Y. Kim, *Chem. Mater.* **2010**, *22*, 587.
- [2] J. W. Choi, D. Aurbach, *Nat. Rev. Mater.* **2016**, *1*, 16013.
- [3] P. Canepa, G. S. Gautam, D. C. Hannah, R. Malik, M. Liu, K. G. Gallagher, K. A. Persson, G. Ceder, *Chem. Rev.* **2017**, *117*, 4287.
- [4] G. Z. Fang, J. Zhou, A. Q. Pan, S. Q. Liang, *ACS Energy Lett.* **2018**, *3*, 2480.
- [5] M. Song, H. Tan, D. L. Chao, H. J. Fan, *Adv. Funct. Mater.* **2018**, *28*, 1802564.

- [6] B. Y. Tang, L. T. Shan, S. Q. Liang, J. Zhou, *Energy Environ. Sci.* **2019**, *12*, 3288.
- [7] G. He, W. H. Kan, A. Manthiram, *Chem. Mater.* **2016**, *28*, 682.
- [8] Z. L. Jian, Y. S. Hu, X. L. Ji, W. Chen, *Adv. Mater.* **2017**, *29*, 1601925.
- [9] P. Barpanda, L. Lander, S. Nishimura, A. Yamada, *Adv. Energy Mater.* **2018**, *8*, 1703055.
- [10] F. Wang, W. Sun, Z. Shadike, E. Y. Hu, X. Ji, T. Gao, X. Q. Yang, K. Xu, C. S. Wang, *Angew. Chem., Int. Ed.* **2018**, *57*, 11978.
- [11] G. L. Li, Z. Yang, Y. Jiang, C. H. Jin, W. Huang, X. L. Ding, Y. H. Huang, *Nano Energy* **2016**, *25*, 211.
- [12] Z. Y. Wu, Y. N. Wang, L. Zhang, L. Jiang, W. C. Tian, C. L. Cai, J. Price, Q. F. Gu, L. F. Hu, *ACS Appl. Energy Mater.* **2020**, *3*, 3919.
- [13] L. F. Hu, Z. Y. Wu, C. J. Lu, F. Ye, Q. Liu, Z. M. Sun, *Energy Environ. Sci.* **2021**, *14*, 4095.
- [14] Z. Y. Wu, C. J. Lu, F. Ye, L. Zhang, L. Jiang, Q. Liu, H. L. Dong, Z. M. Sun, L. F. Hu, *Adv. Funct. Mater.* **2021**, *31*, 2106816.
- [15] H. Y. Shi, Y. Song, Z. M. Qin, C. C. Li, D. Guo, X. X. Liu, X. Q. Sun, *Angew. Chem., Int. Ed.* **2019**, *58*, 16057.
- [16] X. Ji, J. Chen, F. Wang, W. Sun, Y. J. Ruan, L. Miao, J. J. Jiang, C. S. Wang, *Nano Lett.* **2018**, *18*, 6441.
- [17] H. X. Li, T. Jin, X. B. Chen, Y. Q. Lai, Z. A. Zhang, W. Z. Bao, L. F. Jiao, *Adv. Energy Mater.* **2018**, *8*, 1801418.
- [18] U. Nisar, R. A. Shakoob, R. Essehli, R. Amin, B. Orayech, Z. Ahmad, P. R. Kumar, R. Kahraman, S. Al-Qaradawi, A. Soliman, *Electrochim. Acta.* **2018**, *292*, 98.
- [19] W. Li, X. Y. Jing, K. Jiang, D. H. Wang, *ACS Appl. Energy Mater.* **2021**, *4*, 2797.
- [20] W. Zhang, Z. A. Zhang, H. X. Li, D. P. Wang, T. S. Wang, X. W. Sun, J. Q. Zheng, Y. Q. Lai, *ACS Appl. Mater. Interfaces* **2019**, *11*, 35746.
- [21] N. Zhang, F. Y. Cheng, J. X. Liu, L. B. Wang, X. H. Long, X. S. Liu, F. J. Li, J. Chen, *Nat. Commun.* **2017**, *8*, 405.
- [22] Y. A. Wang, F. Ye, Z. Y. Wu, L. Jiang, L. Zhang, L. F. Hu, *ACS Appl. Energy Mater.* **2021**, *4*, 4138.
- [23] F. Wan, Y. Zhang, L. L. Zhang, D. B. Liu, C. D. Wang, L. Song, Z. Q. Niu, J. Chen, *Angew. Chem., Int. Ed.* **2019**, *58*, 7062.
- [24] C. Xia, J. Guo, Y. J. Lei, H. F. Liang, C. Zhao, H. N. Alshareef, *Adv. Mater.* **2018**, *30*, 1705580.
- [25] W. Sun, F. Wang, S. Y. Hou, C. Y. Yang, X. L. Fan, Z. H. Ma, T. Gao, F. D. Han, R. Z. Hu, M. Zhu, C. S. Wang, *J. Am. Chem. Soc.* **2017**, *139*, 9775.
- [26] B. Z. Jiang, C. J. Xu, C. L. Wu, L. B. Dong, J. Li, F. Y. Kang, *Electrochim. Acta.* **2017**, *229*, 422.
- [27] C. Y. Zhu, G. Z. Fang, J. Zhou, J. H. Guo, Z. Q. Wang, C. Wang, J. Y. Li, Y. Tang, S. Q. Liang, *J. Mater. Chem. A* **2018**, *6*, 9677.
- [28] L. T. Ma, S. M. Chen, H. F. Li, Z. H. Ruan, Z. J. Tang, Z. X. Liu, Z. F. Wang, Y. Huang, Z. X. Pei, J. A. Zapien, C. Y. Zhi, *Energy Environ. Sci.* **2018**, *11*, 2521.
- [29] K. X. Huang, Z. G. Yao, K. Sun, K. Y. Chen, J. L. Hu, D. G. Yin, C. L. Li, *J. Power Sources.* **2021**, *482*, 228904.
- [30] Z. G. Yao, Y. F. Yu, Q. P. Wu, M. N. Cui, X. J. Zhou, J. J. Liu, C. L. Li, *Small* **2021**, *17*, 2102168.
- [31] Z. G. Yao, Q. P. Wu, K. Y. Chen, J. J. Liu, C. L. Li, *Energy Environ. Sci.* **2020**, *13*, 3149.
- [32] N. Zhang, F. Y. Cheng, Y. C. Liu, Q. Zhao, K. X. Lei, C. C. Chen, X. S. Liu, J. Chen, *J. Am. Chem. Soc.* **2016**, *138*, 12894.
- [33] W. B. Liu, J. W. Hao, C. J. Xu, J. Mou, L. B. Dong, F. Y. Jiang, Z. Kang, J. L. Wu, B. Z. Jiang, F. Y. Kang, *Chem. Commun.* **2017**, *53*, 6872.
- [34] J. W. Ding, Z. G. Du, L. Q. Gu, B. Li, L. Z. Wang, S. W. Wang, Y. J. Gong, S. B. Yang, *Adv. Mater.* **2018**, *30*, 1800762.
- [35] M. Y. Yan, P. He, Y. Chen, S. Y. Wang, Q. L. Wei, K. N. Zhao, X. Xu, Q. Y. An, Y. Shuang, Y. Y. Shao, K. T. Mueller, L. Q. Mai, J. Liu, J. H. Yang, *Adv. Mater.* **2018**, *30*, 1703725.
- [36] D. Kundu, S. H. Vajargah, L. W. Wan, B. Adams, D. Prendergast, L. F. Nazar, *Energy Environ. Sci.* **2018**, *11*, 881.
- [37] Q. Pang, C. L. Sun, Y. H. Yu, K. N. Zhao, Z. Y. Zhang, P. M. Voyles, G. Chen, Y. J. Wei, X. D. Wang, *Adv. Energy Mater.* **2018**, *8*, 1800144.
- [38] V. Soundharajan, B. Sambandam, S. Kim, M. H. Alfaruqi, D. Y. Putro, J. Jo, S. Kim, V. Mathew, Y. K. Sun, J. Kim, *Nano Lett.* **2018**, *18*, 2402.
- [39] D. Kundu, B. D. Adams, V. Duffort, S. H. Vajargah, L. F. Nazar, *Nat. Energy.* **2016**, *1*, 16119.
- [40] B. Y. Tang, G. Z. Fang, J. Zhou, L. B. Wang, Y. P. Lei, C. Wang, T. Q. Lin, Y. Tang, S. Q. Liang, *Nano Energy.* **2018**, *51*, 579.
- [41] B. Sambandam, V. Soundharajan, S. Kim, M. H. Alfaruqi, J. Jo, S. Kim, V. Mathew, Y. K. Sun, J. Kim, *J. Mater. Chem. A* **2018**, *6*, 3850.
- [42] Y. Q. Yang, Y. Tang, G. Z. Fang, L. T. Shan, J. S. Guo, W. Y. Zhang, C. Wang, L. B. Wang, J. Zhou, S. Q. Liang, *Energy Environ. Sci.* **2018**, *11*, 3157.
- [43] S. C. Liu, H. Zhu, B. H. Zhang, G. Li, H. K. Zhu, Y. Ren, H. B. Geng, Y. Yang, Q. Liu, C. C. Li, *Adv. Mater.* **2020**, *32*, 2001113.
- [44] L. Y. Zhang, L. Chen, X. F. Zhou, Z. P. Liu, *Adv. Energy Mater.* **2015**, *5*, 1400930.
- [45] Z. Liu, G. Pulletikurthi, F. Endres, *ACS Appl. Mater. Interfaces.* **2016**, *8*, 12158.
- [46] Z. G. Hou, X. Q. Zhang, X. N. Li, Y. C. Zhu, J. W. Liang, Y. T. Qian, *J. Mater. Chem. A* **2017**, *5*, 730.
- [47] W. Li, K. L. Wang, S. J. Cheng, K. Jiang, *Energy Storage Mater.* **2018**, *15*, 14.
- [48] J. W. Zhao, Y. Q. Li, X. Peng, S. M. Dong, J. Ma, G. L. Cui, L. Q. Chen, *Electrochem. Commun.* **2016**, *69*, 6.
- [49] V. Verma, S. Kumar, W. Manalastas, J. Zhao, R. Chila, S. Z. Meng, P. Kidkhunthod, M. Srinivasan, *ACS Appl. Energy Mater.* **2019**, *2*, 8667.
- [50] Z. Y. Wu, C. J. Lu, Y. N. Wang, L. Zhang, L. Jiang, W. C. Tian, C. L. Cai, Q. F. Gu, Z. M. Sun, L. F. Hu, *Small.* **2020**, *16*, 2000698.
- [51] P. He, M. Y. Yan, G. B. Zhang, R. M. Sun, L. N. Chen, Q. Y. An, L. Q. Mai, *Adv. Energy Mater.* **2017**, *7*, 1601920.
- [52] H. F. Li, Q. Yang, F. N. Mo, G. J. Liang, Z. X. Liu, Z. J. Tang, L. T. Ma, J. Liu, Z. C. Shi, C. Y. Zhi, *Energy Storage Mater.* **2019**, *19*, 94.
- [53] Q. Zhao, W. W. Huang, Z. Q. Luo, L. J. Liu, Y. Lu, Y. X. Li, L. Li, J. Y. Hu, H. Ma, J. Chen, *Sci. Adv.* **2018**, *4*, eaao176.
- [54] D. Kundu, P. Oberholzer, C. Glaros, A. Bouzid, E. Tervoort, A. Pasquarello, M. Niederberger, *Chem. Mater.* **2018**, *30*, 3874.
- [55] K. W. Nam, H. Kim, Y. Beldjoudi, T. W. Kwon, D. J. Kim, J. F. Stoddart, *J. Am. Chem. Soc.* **2020**, *142*, 2541.
- [56] Z. W. Guo, Y. Y. Ma, X. L. Dong, J. H. Huang, Y. G. Wang, Y. Y. Xia, *Angew. Chem., Int. Ed.* **2018**, *57*, 11737.
- [57] H. Y. Shi, Y. J. Ye, K. Liu, Y. Song, X. Q. Sun, *Angew. Chem., Int. Ed.* **2018**, *57*, 16359.
- [58] C. J. Xu, B. H. Li, H. D. Du, F. Y. Kang, *Angew. Chem., Int. Ed.* **2012**, *51*, 933.
- [59] R. Trocoli, F. La Mantia, *ChemSusChem.* **2015**, *8*, 481.
- [60] F. Chen, V. M. Kovrugin, R. David, O. Mentre, F. Fauth, J. N. Chotard, C. Masquelier, *Small Methods* **2019**, *3*, 1800218.
- [61] Y. Gogotsi, R. M. Penner, *ACS Nano.* **2018**, *12*, 2081.
- [62] Y. Yan, B. Hao, D. Wang, G. Chen, E. Markweg, A. Albrecht, P. SchAAF, *J. Mater. Chem. A* **2013**, *1*, 14507.